

Mechanisms of estuarine salt plug formation by an along-shelf buoyant current: a numerical model approach

Braulio Juarez¹, Arnoldo Valle-Levinson², and Alberto Canestrelli²

¹Instituto de Investigaciones Oceanológicas, Universidad Autónoma de Baja California

²University of Florida

November 26, 2022

Abstract

While estuarine salt plugs can develop worldwide in estuaries adjacent to buoyant coastal currents, their formation has been scarcely documented. This study aims to generalize a mechanism for salt plug formation that does not invoke evaporation processes but involves a buoyant coastal current modified by wind stresses. A numerical model, Delft3D, is used to simulate two idealized bays, one with a single inlet and another with two inlets. The numerical experiments are inspired by recent observations and simulate nine different scenarios of wind and tidal forcings under the influence of an along-shelf buoyant current. Results show that the salt plug induces an inverse circulation at the inlet with inflow at the surface and outflow underneath. This circulation is modified by wind action. The persistence of the salt plug depends on tidal flushing, as well as wind intensity and direction. A yearlong numerical experiment with non-stationary buoyant currents and non-stationary winds indicate that: (i) onshore winds transport oceanic waters into the bay, while offshore winds export estuarine water to the ocean; (ii) onshore winds enhance the inverse circulation at the inlet, while offshore winds stall it. The ratio between wind-driven and density-induced accelerations, given by the Wedderburn number, determines the dominant contribution to the along-estuary circulation in an along-estuary transect. In general, baroclinicity dominates over wind-stress at the inlet, while wind-stress governs the circulation along the estuary. This study represents the first attempt to identify the role of wind and buoyant coastal currents on the dynamics of salt plug formation.

26 governs the circulation along the estuary. This study represents the first attempt to identify the
27 role of wind and buoyant coastal currents on the dynamics of salt plug formation.

28 *Plain Language Summary*

29 A local of maximum salinity within estuaries is usually refer as a salt plug because it obstructs
30 the renovation of water, affecting the water quality of the estuary. Salt plugs can develop
31 worldwide in estuaries adjacent to low-salinity coastal currents, however, their formation has
32 been scarcely documented. This study aims to generalize a mechanism for salt-plug formation
33 due to a low-salinity coastal current and modified by wind action. A numerical model, Delft3D,
34 is used to simulate two idealized bays, one with a single inlet and another with two inlets. The
35 numerical model simulates nine different scenarios of wind and tidal forcings under the influence
36 of a low-salinity coastal current. Results show that the salt plug induces an inflow at the surface
37 and outflow underneath. A yearlong experiment with a temporally varying coastal current and
38 wind indicate that: (i) onshore winds transport oceanic waters into the bay, while offshore winds
39 export estuarine water to the ocean; (ii) onshore winds enhance the inflow at the surface and
40 outflow underneath at the inlet, while offshore winds stall it. This study represents the first
41 attempt to identify the role of wind and low-salinity coastal currents on the dynamics of salt plug
42 formation.

43
44
45
46
47
48
49
50
51
52
53
54
55
56

57
58
59
60
61
62
63
64
65
66
67
68
69
70
71
72
73
74
75
76
77
78
79
80

1. Introduction

Typical estuarine gravitational circulation consists of outflow at the surface and inflow underneath (Pritchard, 1952, 1956; Hansen and Rattray, 1965). Under particular conditions, an estuary can develop a “salt plug”, which is defined as a region of maximum salinity inside the estuary. During salt-plug formation, circulation at the inlet reverses and consists of inflow at the surface and outflow underneath, which is referred to as “inverse circulation”. Salt plugs usually occur in estuaries where evaporation rates are equal or higher than the freshwater input (Largier, 2010). In hypothermal estuaries, in which estuarine water is colder than in the adjacent ocean, a salt plug induces an inverse density gradient between mid-estuary and the ocean, and a positive gradient between mid-estuary and the estuary head. Those opposing gradients drive a surface convergence zone in the salt-plug region that increases flushing times and reduces water quality within an estuary (Largier, 2010). For this reason, it is crucial to understand the conditions that favor salt plug formation.

Salt-plug formation may not be exclusive of low-inflow estuaries, where evaporation rates are mostly dominant in causing the plug. In Barataria Bay, Louisiana, USA, Juarez et al. (2020) recently proposed an alternative mechanism for salt-plug formation that prescind of evaporation. Their observations corroborated numerical results of Li et al. (2011), attributing a local salinity maximum inside the estuary to an along-shore buoyant current that transported brackish water into the estuary. Such transport was modified by the direction of the wind. This formation mechanism also appears in other estuaries. In Willapa Bay, north of the Columbia

81 River, Hickey and Banas (2003) observed a reversal of the salinity gradient between the mid-
82 estuary and the ocean. Such reversal was induced by the intrusion of the Columbia River plume
83 during downwelling (or onshore wind) conditions. Columbia River plume intrusions were also
84 observed at Grays Harbor (Banas et al., 2009) and Strait of Juan de Fuca (Giddings and
85 MacCready, 2017). Numerical simulations in Plum Island Sound, Massachusetts, showed
86 intrusions of the Merrimack River plume into the sound, inducing local salinity maxima (Zhao et
87 al., 2010). These examples correspond to systems adjacent to prototypical plumes (Horner-
88 Devine et al., 2015). However, other types of plumes may contribute to salt-plug formation at
89 adjacent estuaries, such as the Mississippi River that forms a delta-type plume (Horner-Devine et
90 al., 2015).

91 The main goal of this study is to generalize the mechanism described in Juarez et al.
92 (2020) by exploring the contribution of each forcing involved in the salt-plug formation. A
93 numerical model is implemented for an idealized domain to address this goal. The idealized
94 model allows us to isolate the effects caused by wind, tides and buoyant coastal currents, all
95 involved in the salt-plug formation. We consider both the case of an estuary with one and two
96 inlets. The two configurations allow extrapolations of the conclusions to systems with more than
97 one inlet.

98

99 **2. Idealized Numerical Model**

100 **2.1 Model setup and initial conditions**

101 The Delft3D-FLOW numerical model is implemented for estuarine flow in an idealized
102 domain, which consists of a typical bar-built bay with a river centered at the bay head (Figure 1).
103 The bay dimensions and the values of the input parameters (e.g., Coriolis parameter, initial

104 salinity, tidal amplitude, wind speed, buoyant current speed, and salinity) were inspired by recent
105 salt-plug observations in Barataria Bay (Juarez et al., 2020). The model domain consists of a
106 rectangular grid with 362 cross-shelf cells and 122 along-shelf cells. The cell size is 250 m. In
107 the vertical, the domain is discretized using three sigma layers. Earth's rotation is considered,
108 and the Coriolis parameter f is set to $7.05 \times 10^{-5} \text{ s}^{-1}$ (29° of latitude). The domain consists of three
109 regions: the shelf region, the riverine region, and the basin (estuary or bay) region (Figure 1).
110 The shelf region is beyond 61 km and has a constant depth of 10 m. The riverine region extends
111 from $x = 0$ to $x = 30$ km, has a constant depth of 3 m and a width of 2 km. The basin region
112 ranges from $x = 30$ km to $x = 59$ km with a constant depth of 3 m, except in the channels, which
113 are 15 km long and depart from the inlet. The maximum channel depth of 10 m is smoothly
114 connected to the basin depth of 3 m using the Delft3D-QUICKIN module with a smoothing
115 factor of 0.5 and 10 smoothing steps. For more information on the smoothing process, refer to
116 the Delft3D-Flow manual (Deltares, 2014). The basin connects to the shelf by means of 2 km-
117 long inlets (from $x = 59$ km to $x = 61$ km). The model time step is 1 min, and the model runs for
118 150 days, except in Experiment 5, where it runs for 365 days (one year). The initial water level is
119 at mean sea level (0 m). An initial salinity of 30 g/kg is prescribed for the entire domain,
120 consistently with the maximum salinity observed at Barataria Bay in Juarez et al. (2020). This
121 initial salinity value only affects the maximum salinity reached in the salt-plug and how long it is
122 sustained. A k - ε turbulence closure model is used to compute eddy viscosities and diffusivities.

123

124 **2.1. Boundary conditions**

125 Four open boundaries limit the model domain (Figure 1). A constant riverine discharge
126 ($100 \text{ m}^3/\text{s}$) is prescribed at the upstream boundary ($x = 0$ km) with a logarithmic vertical velocity

127 profile. The ocean boundary is parallel to the coast ($x = 90$ km). At that location, the water level
128 is prescribed in the form of a 0.1 m amplitude (micro-tidal) diurnal tide. The third and fourth
129 open boundaries are on the shelf and perpendicular to the coast (blue lines in Figure 1). At these
130 boundaries, a Riemann condition is prescribed, which simulates a southward along-shelf buoyant
131 current with a vertically uniform velocity of 0.1 m/s. As for the salinity, it is set to zero at the
132 river boundary (freshwater inflow). It is set to 20 g/kg at the boundaries perpendicular to the
133 coast so that the buoyant along-shore current transports brackish water into the domain. A
134 salinity of 30 g/kg is prescribed at the seaward boundary.

135

136 **2.2.Numerical Experiments**

137 A total of nine numerical experiments were run, in which we assessed the relative
138 contributions of three forcings driving the transport and dispersion of salt in the model domain:
139 along-shelf coastal current, tides, and cross-shore winds. Experiments 1 to 4 consider a single
140 inlet in the axis of the basin ($y = 15$ km) and an along-shelf buoyant coastal current (Figure 1).
141 The next four experiments, 1T to 4T, consider two inlets with the axis at $y = 10$ km and $y = 20$
142 km (Figure 1). Inlets have an opening width of 2 km and a cross-shore length of 2 km. All
143 experiments include an upstream river discharge. Experiments 1 and 1T consider no tide or wind.
144 Interactions between tide and coastal current are simulated in Experiments 2 and 2T.
145 Experiments 3 and 3T include tides and a steady offshore wind of 5 m/s. Experiments 4 and 4T
146 include tides and a steady onshore wind of 5 m/s. The magnitudes of these forcings are similar to
147 the one measured in Barataria Bay by Juarez et al. (2020).

148 Experiment 5 lasts one year and consists of a simulation with non-stationary coastal
149 current and wind. The periodicity of the coastal current and the shift in wind direction are

150 inspired by the seasonality observed in the Barataria Bay area (Juarez et al., 2020). The coastal
151 current velocity is set to a constant value of 0.1 m/s at the beginning of the simulation under no
152 wind conditions. After day 180, the coastal current is turned off (velocity equal to 0 m/s), and an
153 offshore wind is turned on. After day 273, the coastal current velocity is turned on again to 0.1
154 m/s, and the wind direction switches to onshore. These conditions persist until the end of the
155 simulation.

156

157 **2.3. Model Output Analysis**

158 All the outcomes are filtered using a Lanczos low-pass filter with a cut-off period of 48
159 hrs to remove tidal and inertial oscillations. Hovmöller diagrams are used to describe model-
160 related variables that change in space and time. In this study, the axes of the Hovmöller diagrams
161 represent along-channel distance (x-axis) and simulation time (y-axis). Hovmöller diagrams
162 analyze the temporal variation of the subtidal surface salinity for the entire period. Along-
163 channel (x-component) subtidal velocities are drawn near the surface and bottom at a grid point
164 (see Figure 1) at the center of the inlet(s). Finally, we present maps of tidally averaged surface
165 salinity and velocity vectors during periods of inverse circulation at the inlet.

166

167 **3. Results**

168 Results are presented into three subsections. First, we consider steady scenarios with a
169 single inlet. Then, steady scenarios with two inlets. Finally, we consider an unsteady case with
170 two inlets. Each subsection first presents Howmoller diagrams of salinity distributions, followed
171 by time series of surface and bottom velocities centered at the inlet, and concluding with maps of
172 surface velocity and salinity fields.

173

174 **3.1. Single Inlet Experiments**

175 Single-inlet experiments show the formation of a salt plug that induces an inverse
176 circulation at the inlet. A Hovmöller diagram of the along-estuary salinity distribution shows a
177 salt-plug formation in all four cases: no tide and no wind (Figure 2a), tide and no wind (Figure
178 2b), tide plus offshore wind (Figure 2c), and tide plus onshore wind (Figure 2d). After 30 days of
179 simulation, salinity reaches maximum values of ~ 24 g/kg inside the bay and ~ 22 g/kg at the inlet
180 in Experiments 1, 2, and 4. The relative maximum of salinity inside the bay lasts ~ 60 days, with
181 the maximum always located between the bay head ($x = 30$ km) and the inlet, and with salinity
182 values decreasing through time. From day 90 to the end of the simulation, the along-estuary
183 salinity values decrease from the head, < 12 g/kg, to the inlet > 19 g/kg. In experiment 3 (Figure
184 2c), a local of maximum salinity inside the bay is not clearly noticeable in the Hovmöller
185 diagram representation as in the surface map discussed below. The maximum salinity > 28 g/kg
186 is observed during the entire simulation and even covering a region in the ocean domain near the
187 bars from $x = 61$ km to $x = 65$ km, approximately.

188 Salt-plug formation affects the circulation at the inlet. During the period in which the salt
189 plug is present, surface, and bottom velocities at the inlet depict an inverse circulation with
190 inflow at the surface and outflow underneath (Figure 3). Inverse circulation disappears in
191 experiment 3, which is forced by tide and offshore wind (Figure 3). The inverse circulation is
192 most vigorous in the case with no tide and no wind (Experiment 1, Figure 3a), reaching values of
193 > 0.2 m/s close to surface and > 0.1 m/s near the bottom. In the case of tide and offshore wind
194 forcing (Experiment 3, Figure 3c), downwind flow persists at the inlet during the entire
195 experiment. In this case, the circulation is positive indicating a possible wind stress dominance

196 over density gradients. This competition between wind stress and density gradients is explored
197 further in section 4.2. The inverse circulation persists longer in Experiment 4 (Figure 2d, tide
198 plus onshore wind) than in Experiments 1 and 2. In Experiment 4, the inverse circulation is
199 present during the entire experiment. However, the inverse circulation after day 90 may be wind-
200 induced because it follows the onshore wind at the surface (inflow) and displays a compensating
201 flow in the opposite direction (outflow) near the bottom.

202 Surface maps of salinity and velocity show the spatial structure of the salt-plug and the
203 associated velocities. Day 44 of the simulation is chosen arbitrarily for these maps because the
204 salt plug is present at that time in all the experiments (vertical line in Fig. 3). The horizontal
205 distribution with no tide and no wind (Figure 4a) indicates a maximum salinity zone of ~ 24 g/kg
206 that extends between $x \sim 40$ km and $x \sim 57$ km. Laterally, this zone expands up to ~ 10 km. The
207 tidally averaged flow is directed landward at the inlet and slightly deflected northward. Outflow
208 develops at the southern end of the bay with velocities of ~ 0.1 m/s. At the salt-plug zone,
209 velocities are < 0.05 m/s. By adding tides (Figure 4b) the high salinity zone shows a lateral
210 expansion relative to the case of no tides and winds. Also, tides favor the intrusion, up to $x \sim 50$
211 km (10 km intrusion), of a plume of brackish water with salinity ~ 22 g/kg from the along-shelf
212 current. The high salinity zone reaches salinities up to 24 g/kg inside the bay, where the flow
213 velocity is close to zero.

214 The inclusion of offshore wind and tides induces a high salinity zone inside the bay
215 (Figure 4c). The salt plug under the forcing of tides and offshore wind has the highest salinity
216 values, up to ~ 30 g/kg. Surprisingly, inflows in correspondence of the salt plug axis are the
217 largest ones in the bay, which contrasts with the near-stagnant conditions at the salt plug for the
218 cases with no wind (Experiments 1 and 2). The direction of the flow within the bay follows

219 theoretical considerations indicating downwind flow over shoals and upwind flow in the channel
220 (e.g., Csanady, 1973; Wong, 1994). An offshore wind opposes the buoyant coastal current in
221 transporting brackish water into the bay. This response causes relatively high salinity water to
222 remain enclosed and recirculating inside the bay. The experiment with onshore winds (Figure 4d)
223 also develops a salt plug. Similarly to the experiment with offshore winds (Figure 4c), the
224 highest outflows appear in the salt-plug region. Again, the residual circulation inside the bay
225 follows theoretical expectations of wind-driven flows over shoal-thalweg bathymetry. The
226 salinity inside the bay is lower than in the simulation with offshore winds (Experiment 3).

227 The results indicate that a salt plug may appear from an along-shelf buoyant current that
228 intrudes into a single-inlet system. Whether this buoyant water intrusion may develop in systems
229 with two or more inlets is still unknown. The next subsection explores the features of a salt plug
230 in a bay with an additional inlet, under the same forcing conditions.

231

232 **3.2. Two-inlet Experiments**

233 Experiments in section 3.1 are repeated for a bay with two inlets. Hovmöller diagrams of
234 surface salinity along the thalweg at both inlets (Figure 5) display similar distributions compared
235 to the single-inlet experiment (Figure 2). The most marked differences are observed in the
236 magnitudes of the velocities and the maps of surface salinity and velocity. The ocean-bay
237 circulation structure changes due to the extra inlet. In general, surface, and bottom velocities are
238 higher than the velocities computed in the case of a single inlet. Bottom and surface along-
239 estuary velocities at the center of the two inlets (dots in Figure 1) show an inverse circulation in
240 Experiments 1T (Figure 6a), 2T (Figure 6b), and 4T (Figure 6d). The inverse circulation that
241 develops under no tide and no wind (Experiment 1T), and with tides (Experiment 2T) lasts less

242 than the circulation resulting from an onshore wind (Experiment 4T). Offshore wind in
243 Experiment 3T enhances a positive circulation at both inlets with bottom velocities higher than
244 surface velocities at the northern inlet and the opposite at the southern inlet. Moreover, the
245 onshore wind enhances the inflow at the surface, which reaches values up to 0.3 m/s. At the
246 inlets, offshore winds prevent the inverse circulation, and onshore winds enhance and prolong
247 the inverse circulation.

248 Tidally averaged surface salinity and velocity maps (Figure 7) are shown for day 44 of
249 the simulation (see the vertical line in Figure 6). The experiments with no tide and no wind
250 (Experiment 1T, Figure 7a) and with tide (Experiment 2T, Figure 7b) display a maximum
251 salinity zone in the southern portion of the bay. This zone exhibits a maximum salinity of ~ 24
252 g/kg at $x \sim 52$ km, which is the core of a cyclonic gyre with a radius of ~ 10 km. This cyclonic
253 circulation becomes more evident with tides only (Experiment 2T). Although winds modify the
254 circulation (Experiments 3T and 4T), the salt plug remains in the bay. The influence of offshore
255 wind (Experiment 3T) results in a region of maximum salinity that coincides with the location of
256 the thalweg and is surrounded by relatively low-salinity waters (~ 26 g/kg). The mean flow fields
257 indicate upwind circulation in the thalweg, and downwind over the shallowest region of the bay.
258 This flow pattern agrees with the classical wind-driven theory and generates a re-circulation
259 trapping salty water inside the bay. Outside the bay, the salinity remains higher than 28 g/kg, and
260 the outflow from the southern inlet of ~ 0.2 m/s is strong enough to stall the inflow of the
261 brackish water from the buoyant coastal current. Onshore winds (Experiment 4T) cause an
262 accumulation of high-salinity (~ 25 g/kg) water at the southwestern portion of the bay. The wind
263 blowing from the sea to the bay enhances the transport of low-salinity (~ 22 g/kg) water from the
264 coastal current. Upwind flow of ~ 0.2 m/s in the thalweg of both channels opposes weaker (~ 0.1

265 m/s) downwind inflow over shoals. This residual flow changes direction approximately 2 km
266 from the inlet. In general, the salt plug was persistent until the water inside the bay was
267 homogenized to brackish water by the steady coastal current.

268

269 **3.3.Unsteady effects**

270 Here we present the results for experiment 5, for which we prescribe a relaxation in the
271 along-shelf buoyant current that allows oceanic water to enter the bay. Experiment 5 included
272 tides, non-steady wind forcing, and a non-steady along-shelf buoyant current (see section 2.2).
273 This experiment shows the same results as experiment 2T (tides and no wind) until the coastal
274 current is turned off on day 180 (not shown). By day ~180, salinity displays the same along-
275 estuary distribution as the experiment with only tides (Figure 5b), with a salinity of ~ 20 g/kg
276 near the inlet (Figure 8). After day 210 waters with salinity > 20 g/kg enter the bay up to ~15 km
277 from the inlet. Offshore winds favor intrusion of waters with a salinity of 24 g/kg up to 20 km
278 from the inlet. Offshore winds also drive buoyant waters away from the inlet, favoring an
279 upwind flow deeper in the channel that imports oceanic saltier water into the bay. By day 270,
280 the salinity contour of 24 g/kg reaches 10 km into the bay. After day 270, the buoyant coastal
281 current is turned on, trapping salty water (>22 g/kg) inside the bay. By day 280, the salinity in
282 the bay is higher than at the inlet. Onshore winds extend the duration of the salt plug in the bay,
283 which persists until day 330 in the northern inlet and until day 310 in the southern inlet.

284 Surface and bottom subtidal velocities (Figure 9) centered at both inlets show two
285 reversals in the estuarine circulation. The first reversal occurs similarly to that described for
286 steady forcing with only tides (Experiment 4T). By day 181, when the buoyant current is turned
287 off, the gravitational exchange, or positive circulation, increases from ~0.05 m/s to >0.1 m/s at

288 the surface and the bottom. Offshore winds enhance the positive circulation at the inlet,
289 increasing the outflow at the surface from ~ 0.05 m/s to >0.2 m/s, and the inflow at the bottom
290 from ~ -0.05 m/s to ~ 0.2 m/s. The second reversal of circulation occurs when both the onshore
291 wind and the buoyant current are turned on. The onshore wind increases the water velocities up
292 to >0.1 m/s and >0.2 m/s at the surface and the bottom, respectively, and also extends the period
293 of inverse circulation until the last week of simulation.

294 Figure 10 shows maps of tidally averaged surface flow and salinity for day 257 with no
295 coastal current (black line in Figure 9) and on the day with the highest outflow at the surface (red
296 line in Figure 9). Inside the bay, two regions of maximum salinity formed at $y \sim 20$ km and $y \sim 7$
297 km, for the case of offshore winds with no coastal current (Figure 10a) and onshore winds with a
298 coastal current (Figure 10b), respectively. The salt plug in the northern bay is saltier (~ 26 g/kg)
299 than in the south (~ 24 g/kg). Inside the bay, the flow is mostly wind-induced, with downwind
300 velocities over the shoals, upwind velocities in the channels, and outflow at both inlets. When the
301 wind reverses to onshore-directed and the coastal current is turned on, the salinity at the inlet
302 decreases to ~ 22 g/kg, while the salinity at the inner bay is ~ 24 g/kg. The circulation inside the
303 bay is still wind-driven, with a ~ 0.2 m/s inflow at the inlet. Therefore, wind enhances the
304 gravitational circulation at the inlet.

305

306 **4. Discussion**

307

308 **4.1. The Mississippi River plume scenario**

309 The steady-state experiments depicted in sections 3.1 and 3.2 resemble the scenario in
310 which freshwater pulses from an along-shelf buoyant current affects a single inlet and two inlet

311 system. Our results described a steady buoyant current that homogenized the salinity inside the
312 bay after ~ 90 to 120 days of simulation. In reality, the Mississippi River spawns an unsteady
313 along-shelf buoyant current (the Louisiana Coastal Current), which affects a multiple-inlet
314 system (Barataria Bay). The buoyant coastal current may experience relaxation periods since it is
315 linked to the Mississippi River seasonality (Rouse and Inoue, 2005). Relaxation periods result in
316 a decrease in brackish water intrusion into the bays adjacent to the delta (Juarez et al., 2020),
317 thus increasing the average salinity in the bays. On the northwestern U.S. coast, the fate of the
318 Columbia River plume is also linked to seasonality in wind forcing. During onshore or
319 downwelling wind conditions, the intrusion of coastal plume waters into estuaries located north
320 of the river mouth causes inverse estuarine circulation at the entrance of these systems (e.g.
321 Banas 2009; Hickey and Banas, 2003; Giddings and MacCready 2017). To understand the
322 importance of unsteady effects, in section 3.3 we discussed results from an experiment that
323 considered a non-steady buoyant coastal current and wind variability similar to what has been
324 observed in the Mississippi River delta. Results showed that the buoyant inner-shelf current
325 functions as a trap of salty water inside the bay. Salty waters enter the bay during buoyant
326 current relaxation times. Wind action may enhance or reduce trapping depending on its direction.
327 Offshore winds drive the inner-shelf buoyant waters seaward. Under this forcing, the bay may
328 still import salty water through the thalweg following wind-driven theory (Wong 1994; Geyer
329 1997). Onshore winds enhance the inverse circulation at the inlets and the brackish water
330 transport from the along-shelf current toward the bay. These results agreed with observations
331 described at Barataria Bay in the Mississippi River Delta (Juarez et al., 2020), and the
332 observations and numerical results of the bays to the north of the Columbia River (Hickey and
333 Banas, 2003; Banas et al., 2009; Giddings and MacCready, 2017).

334

335 **4.2. Differences between single inlet and two inlets**

336 Salt plugs are form in both idealized configurations, thus suggesting that salt-plug
 337 formation may occur at any system adjacent to a buoyant current independently of the number of
 338 inlets. However, single-inlet and two-inlets experiments display differences in the velocities and
 339 the surface salinity. The extra opening in the two-inlet experiments increases the magnitudes of
 340 tidally-averaged velocities at the inlets with respect to the experiments with one inlet (Figure 3
 341 and Figure 6). With two inlets, since the tidal prism per inlet is smaller, a smaller volume of
 342 water is exchanged with the sea at each tidal cycle, and smaller instantaneous depth-averaged
 343 velocities establish at the inlet. As a consequence, vertical mixing is reduced, which
 344 enhances stratification and baroclinic circulations. As a consequence, the tidally-averaged
 345 velocities are larger in the two-inlet case. Experiments with two inlets show lower salinity waters
 346 than one inlet experiments. The mean of the tidally-averaged surface salinity (Figure 4)
 347 calculated for the entire bay domain (bay-averaged) ($30 \text{ km} < x < 60 \text{ km}$) with one inlet,
 348 experiments 1, 2, 3, and 4 is 22.63, 23.46, 27.76, and 23.19 g/kg, respectively. Meanwhile, mean
 349 salinity for the bay domain with two inlets, experiments 1T, 2T, 3T, and 4T (Figure 7), is 21.52,
 350 21.57, 27.60, and 21.74 g/kg, respectively.

351

352 Salt flux through each inlet section computed for experiments with one and two inlets
 353 characterizes exchange processes through the salinity transport. Following Lerczak et al. (2006),
 354 the subtidal salt flux is defined as:

$$F = \langle \int us \, dA \rangle, \quad (1)$$

355 where u is the velocity perpendicular to the inlet, s is the salinity and A is a cross-sectional area.
 356 The angled brackets denote a tidal low-pass filter (or tidal averages). For two inlets, the salt flux
 357 at the northern inlet is added to the flux at the southern inlet. Differences between the fluxes at
 358 the cases with one inlet (F_1) and with two inlets (F_2) are computed ($\Delta F = F_2 - F_1$). In addition,
 359 the difference between the bay-averaged surface salinity with one inlet (\widehat{s}_1) and two inlets (\widehat{s}_2) is
 360 calculated as:

$$\Delta S = \widehat{s}_2 - \widehat{s}_1, \quad (2)$$

361 where the hat, $\widehat{}$, denotes the mean for the entire bay domain. When $\Delta S > 0$, bay-averaged
 362 salinity with two inlets is higher than that with one inlet. On the other hand, when $\Delta S < 0$ bay-
 363 averaged salinity at two inlets is higher than that with one inlet. All the experiments, but the
 364 experiments with offshore wind, show the same relation between salt fluxes and differences in
 365 bay-averaged salinities (Fig. 11). When $\Delta F > 0$ (blue line in Figure 11) the salt flux is larger in
 366 the experiment with two inlets and coincides with $\Delta S < 0$. When ΔS reaches its minimum
 367 (vertical black line in Figure 11), $\Delta F \sim 0$, i.e., the salt flux from the two cases is nearly the same.
 368 When $\Delta F < 0$ the salt flux with one inlet is higher than that with two inlets and ΔS tends to
 369 decrease. These results explain why the salinities in the cases with two inlets are lower than with
 370 one inlet. The salinity transport through the inlets is seaward because salt fluxes are positive in
 371 both cases (not shown). Moreover, salt fluxes with two inlets are higher than with one inlet when
 372 $\Delta F > 0$, yielding an enhanced seaward flushing of saltier water. Experiments with offshore wind
 373 follows different response (Figure 11c). Values of ΔF and ΔS oscillates around zero, meaning
 374 that the basin is insensitive to the number of inlets when forced by an offshore wind.

375

376 **4.3. Wind and density gradients as the dominant forcing**

377 The wind role on the buoyant inner-shelf currents and the volume exchange at the inlets is
 378 twofold. First, it favors or hinders the transport of brackish water from the inner-shelf into the
 379 bay. Second, it enhances or stalls the estuarine circulation. Indeed, wind forcing may dominate
 380 over density gradients in causing the observed subtidal circulation. The Wedderburn number
 381 (Monismith, 1986; Geyer 1997) can be used as indicator of the relative contribution of the two
 382 effects since it is defined as the ratio between the wind-stress and the horizontal density
 383 gradients:

$$W = \frac{\tau_y L}{g \Delta \rho H^2}, \quad (3)$$

384
 385 where τ_y is the along-estuary wind-stress component ($\tau_y = 0.04 \text{ Pa}$, corresponding to a wind
 386 speed of 5 m/s), L is a length scale such as the wind fetch, g is the gravitational acceleration, $\Delta \rho$
 387 is the along-estuary density difference, and H is the water depth. Wind-stresses drive the
 388 circulation if $\log_{10}(W) \gg 0$, and the circulation is driven by density gradients if $\log_{10}(W) \ll 0$.
 389 Here we compute a local value of W by setting L equal to the grid size and $\Delta \rho$ equal to the
 390 density difference between adjacent cells. The $\log_{10}(W)$ was calculated for a transect centered
 391 at the northern thalweg and presented as a Hovmöller diagram in a similar way as the along-
 392 estuary salinity diagrams (see Figures 2, 5, 6, and 10). The Hovmöller diagrams for the southern
 393 thalweg showed similar results as the northern thalweg. Hence, we only report the diagrams for
 394 the northern thalweg.

395 Density gradients drive the residual circulation at the inlet ($x \sim 60 \text{ km}$) in most experiments
 396 (Figure 12) because $\log_{10}(W) < 0$. In experiments with steady offshore winds (Experiments 3,
 397 and 3T; Figure 12a and 12c), wind stress dominates over density gradients in the thalweg (45 km
 398 $< x < 60 \text{ km}$). At $30 \text{ km} < x < 45 \text{ km}$, the $\log_{10}(W) \sim 0$, with a slight dominance of negative

399 values. This implies dominance of density gradients. However, wind effects are non-negligible.
400 Experiments with a steady onshore wind (Experiments 4, and 4T; Figure 12b and 12d) also show
401 wind dominance along the thalweg. From the channel end to the bay head ($30 \text{ km} < x < 45 \text{ km}$)
402 there is a narrow region where baroclinic forces dominate the wind stresses ($\log_{10}(W) < 0$).
403 From $x = 35 \text{ km}$ to $x = 45 \text{ km}$, the wind stresses dominate over the density gradients due to the
404 high friction of this shallow region ($H = 3 \text{ m}$). Baroclinic dominance observed from $x = 30 \text{ km}$ to
405 $x \sim 35 \text{ km}$ is linked to the salinity front observed in the Hovmöller diagrams (Figures 2d and 5d).

406 The experiment with unsteady wind forcing (Figure 12e) showed values of $\log_{10}(W)$
407 consistent with the ones observed for Experiment 3T and 4T (Figures 12c and 12d). From day
408 180 to 271, when there was no buoyancy current and with offshore wind, the along-estuary
409 distribution of $\log_{10}(W)$ was similar to Experiment 3T. Density gradients induced residual
410 circulation from the inlet ($x \sim 60 \text{ km}$) to $x \sim 55 \text{ km}$, wind-stresses dominated the circulation in
411 the thalweg. A region from the channel end to the bay's head seemed to be slightly dominated by
412 the density gradients. From day 272 to the end of the simulation, when the buoyant current is
413 active and an onshore wind is present, the distribution of $\log_{10}(W)$ is similar to Experiment 4T
414 (Figure 12d). Density gradients also dominate the circulation at the inlet ($x \sim 60 \text{ km}$). Wind
415 stresses induce the circulation observed in the thalweg. A narrow region at $x \sim 45 \text{ km}$ is density-
416 driven, followed by another wind-driven region from $x \sim 35 \text{ km}$ to $x \sim 45 \text{ km}$. At the bay's head,
417 from $x = 30 \text{ km}$ to $x \sim 35 \text{ km}$, density gradients induce the residual circulation.

418 This analysis determined the spatial distribution of the dominant drivers of the along-estuary
419 circulation. In the thalweg, the velocity directions followed the wind-driven circulation, with an
420 upwind flow in the channel where density gradients were small. At the inlet, the observed
421 circulation was density-driven and modified by wind stresses.

422

423 **5. Conclusion**

424 The key finding of this study is that an estuarine salt plug can be formed by an along-
425 shelf buoyant current by modifying the circulation between a semi-enclosed basin and the
426 adjacent ocean. The trapped water forms a salt plug and induces an inverse circulation at the
427 inlet. The salt-plug formation occurs independently of whether the basin has one or two inlets.
428 Such salt-plug formation has been observed in other estuaries where evaporation rates may be
429 neglected.

430 Wind forcing plays a secondary role that enhances or hinders the salt-plug formation.
431 Offshore winds drive the buoyant current seaward and set up a circulation that allows inflow of
432 salty water into the channel. Onshore winds enhance the transport of brackish waters into the
433 bay, increase the trapping of salty water, and strengthen the inverse circulation at the inlet.

434 The numerical results described in this study set a baseline to explore the mechanisms of
435 estuarine salt plug formation through a buoyant along-shelf current. This study may be extended
436 in four possible directions. First, the number of inlets could be increased, although we expect that
437 a bay with multiple (>2) inlets should produce similar results, also, the sensitivity to the
438 geometry and depth should be investigated. Second, the ratio between along-shelf current
439 velocities and upstream freshwater velocities should be varied, since this would affect the
440 conditions needed to trap salty water inside the bay. Third, more experiments can be designed to
441 find the different wind conditions that favor salt plug formation or, on the contrary, prevent its
442 formation even in the presence of a buoyant current. Fourth, tidal forcing in this study was small
443 (amplitude = 0.1 m) to represent specific conditions in Barataria Bay (Juarez et al., 2020).

444 Therefore, future studies should investigate the impact of increased tidal flushing on salt plug
445 formation.

446

447 **Acknowledgments**

448

449 This study was funded by the National Science Foundation project (OCE-0825826, OCE-
450 0825833, and OCE-0825876) and by a grant from The Gulf of Mexico Research
451 Initiative/CARTHE II. Funding for Braulio was provided by CONACYT, Mex., under
452 fellowship No. 439858. The model input files are available at [10.6084/m9.figshare.12374840](https://doi.org/10.6084/m9.figshare.12374840).

453

454

455 **References**

456

457 Banas, N. S., MacCready, P., & Hickey, B. M. (2009). The Columbia River plume as cross-shelf
458 exporter and along-coast barrier. *Continental Shelf Research*, 29(1), 292-301.

459 Deltares, D. (2014). *Delft3D-FLOW Simulation of Multi-Dimensional Hydrodynamic Flows and*
460 *Transport Phenomena Including Sediments, User Manual*.

461 Geyer, W. R. (1997). Influence of wind on dynamics and flushing of shallow estuaries.
462 *Estuarine, Coastal and Shelf Science*, 44(6), 713-722.

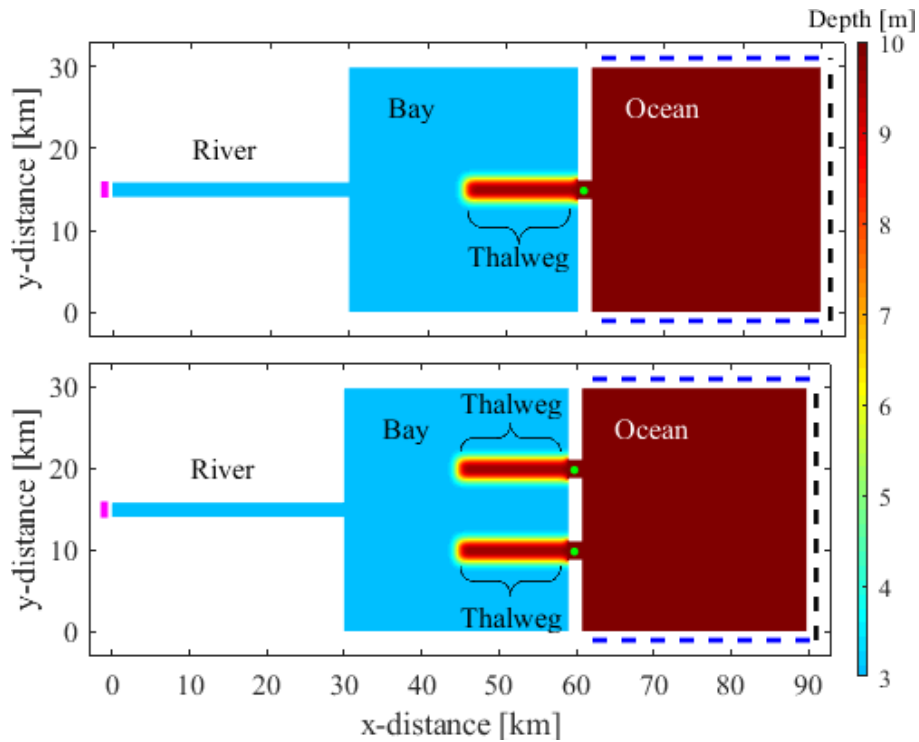
463 Giddings, S. N., & MacCready, P. (2017). Reverse Estuarine Circulation Due to Local and
464 Remote Wind Forcing, Enhanced by the Presence of Along-Coast Estuaries. *Journal of*
465 *Geophysical Research: Oceans*, 122(12), 10184-10205.

466 Hansen, D. V., & Rattray Jr, M. (1966). Gravitational circulation in straits and estuaries, *J. Mar.*
467 *Res.*, 23, 104-122, 1965.

- 468 Hickey, B.M., Banas, N.S. (2003). Oceanography of the US Pacific northwest coastal ocean and
469 estuaries with application to coastal ecology. *Estuaries* 26,1010–1031.
- 470 Horner-Devine, A. R., Hetland, R. D., & MacDonald, D. G. (2015). Mixing and transport in
471 coastal river plumes. *Annual Review of Fluid Mechanics*, 47, 569-594.
- 472 Juarez, B., Valle-Levinson, A., & Li, C. (2020) Estuarine salt-plug induced by freshwater pulses
473 from the inner shelf. *Estuarine Coastal and Shelf Science*,.232, 106491.
- 474 Largier, J. L. (2010). Contemporary issues in estuarine physics, chapter Low-inflow estuaries:
475 hypersaline, inverse, and thermal scenarios. Cambridge University Press.
- 476 Lerczak, J. A., Geyer, W. R., & Chant, R. J. (2006). Mechanisms driving the time-dependent salt
477 flux in a partially stratified estuary. *Journal of Physical Oceanography*, 36(12), 2296-2311.
- 478 Li, C., White, J. R., Chen, C., Lin, H., Weeks, E., Galvan, K., & Bargu, S. (2011). Summertime
479 tidal flushing of Barataria Bay: Transports of water and suspended sediments. *Journal of*
480 *Geophysical Research: Oceans*, 116(C4).
- 481 Monismith, S. (1986). An experimental study of the upwelling response of stratified reservoirs to
482 surface shear stress. *Journal of Fluid Mechanics*, 171, 407-439.
- 483 Pritchard, D. W. (1952). Salinity distribution and circulation in the Chesapeake Bay estuarine
484 system. *J. Mar. Res*, 11, 106-123.
- 485 Pritchard, D. W. (1956). The dynamic structure of a coastal plain estuary. *J. Mar. Res*, 15(1), 33-
486 42.
- 487 Wong, K. C. (1994). On the nature of transverse variability in a coastal plain estuary. *Journal of*
488 *Geophysical Research: Oceans*, 99(C7), 14209-14222.
- 489 Zhao, L., C. Chen, J. Vallino, C. Hopkinson, R. C. Beardsley, H. Lin, and J. Lerczak (2010),
490 Wetland-estuarine-shelf interactions in the Plum Island Sound and Merrimack River in the
491 Massachusetts coast, *Journal of Geophysical Research*., 115, C10039.

492

493



494

495

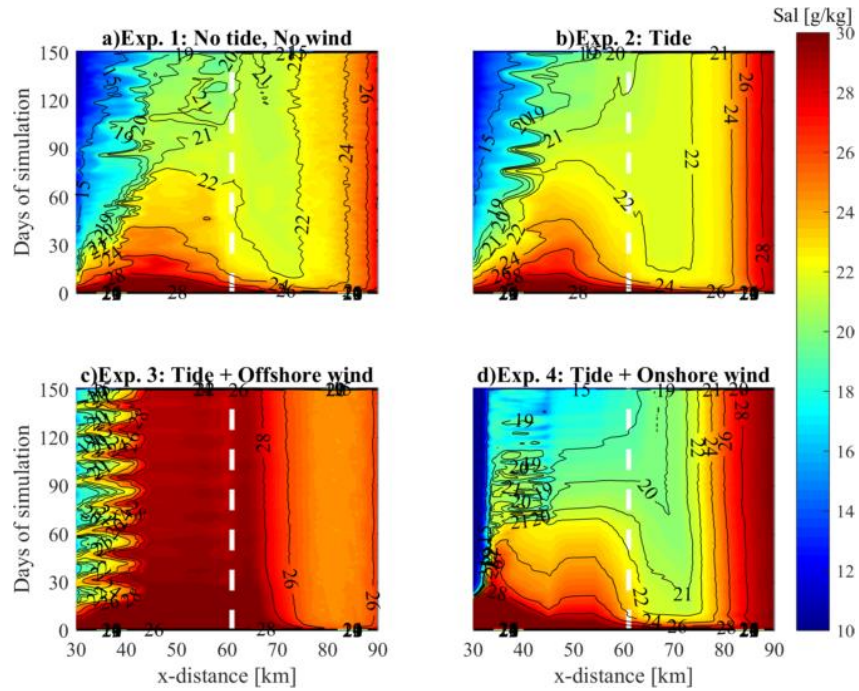
496 Figure 1. Numerical domain. Upper plot: Domain with a single inlet. Lower plot: Domain with
 497 two inlets. The blue dashed lines denote the Riemman open boundaries, black dashed
 498 lines denote water level open boundaries, and the magenta lines denote the river
 499 discharge boundary. The green dots indicate the locations at which the velocities are
 500 sampled (Figures 3, and 6).

501

502

503

504



505

506

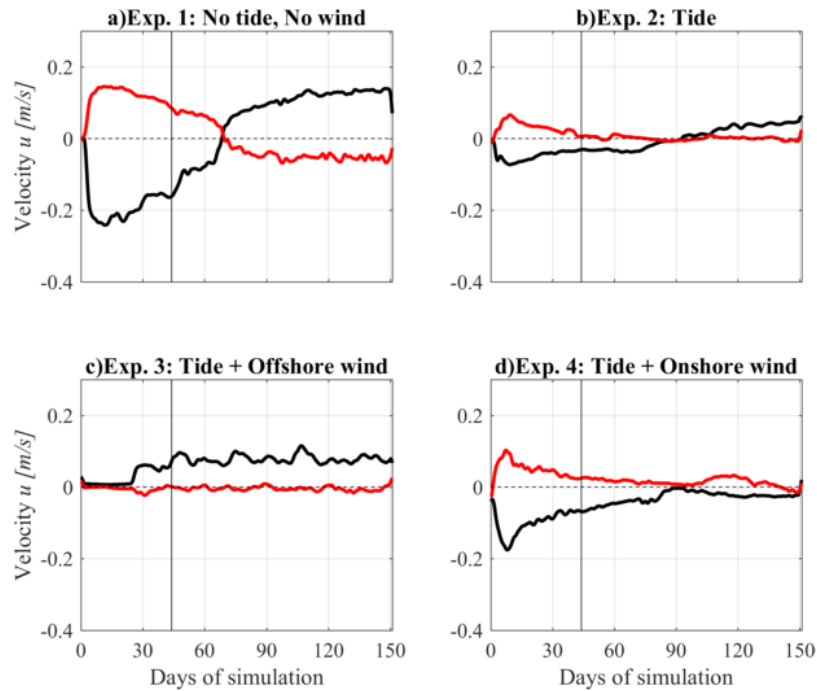
507 Figure 2. Experiments 1 to 4. Hovmöller diagram of surface salinity in a transect which passes
508 through the channel centerline. Upper plot: No wind and no tide (left), and tide, no
509 wind (right). Lower plot: With tides plus offshore wind (left), and onshore wind
510 (right). The vertical dashed white line denotes the location of the northern inlet.

511

512

513

514



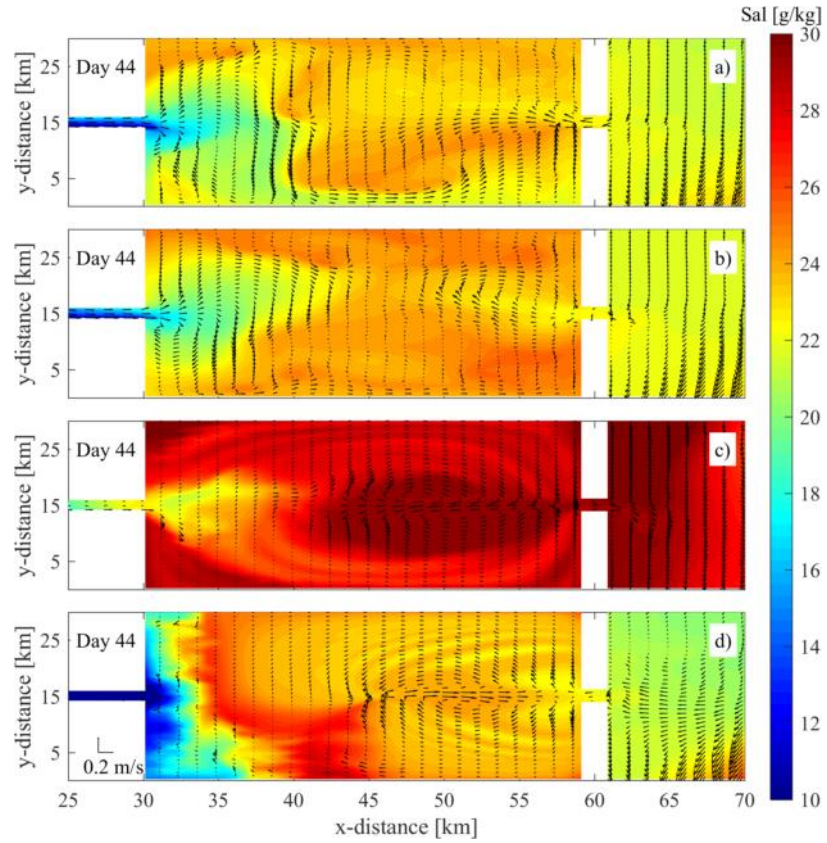
515

516

517 Figure 3. Experiments 1 to 4. Surface (u_s , black) and bottom (u_b , red) subtidal along-estuary
 518 velocities centered at the inlet ($x \sim 65$ km). Velocity is positive seaward. Experiment
 519 with no wind is on a) and with a time-varying wind on b) panel. The vertical solid
 520 line denotes the time used for Figure 4-7.

521

522



523

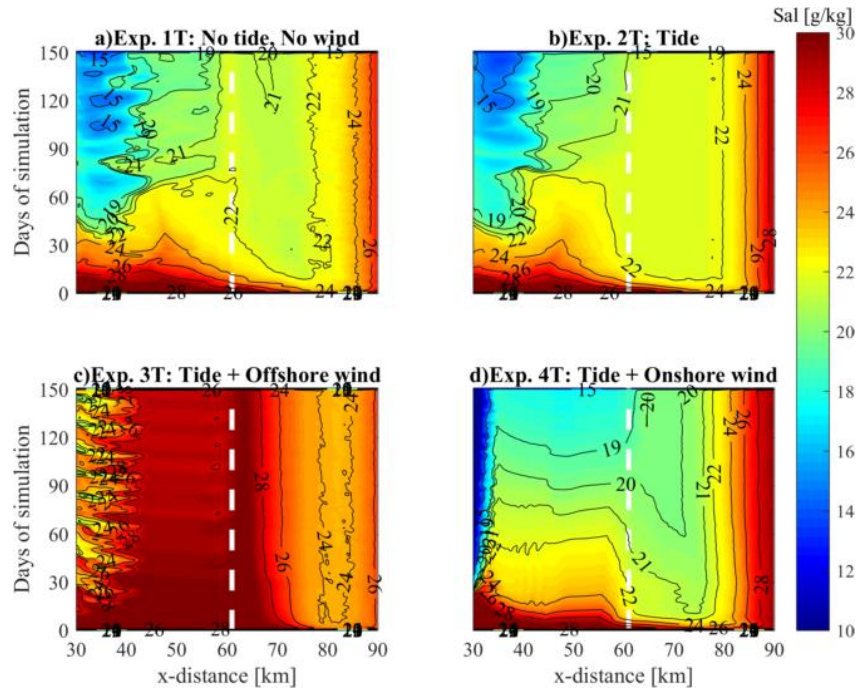
524

525 Figure 4. Experiments 1 to 4. Tidally averaged surface fields of salinity (contour colors), and
526 horizontally velocity (arrows).

527

528

529



530

531

532 Figure 5. Experiments 1T to 4T. Hovmöller diagram of along-estuary surface salinity centered at
 533 the northern channel. a) No wind and no tide, b) tide, no wind, c) tide plus offshore
 534 wind, d) tide plus onshore wind, e) tide plus an upwelling favorable wind, and f) tide
 535 plus a downwelling favorable wind. The white vertical dashed line denotes the
 536 location of the northern inlet.

537

538

539

540

541

542

543

544

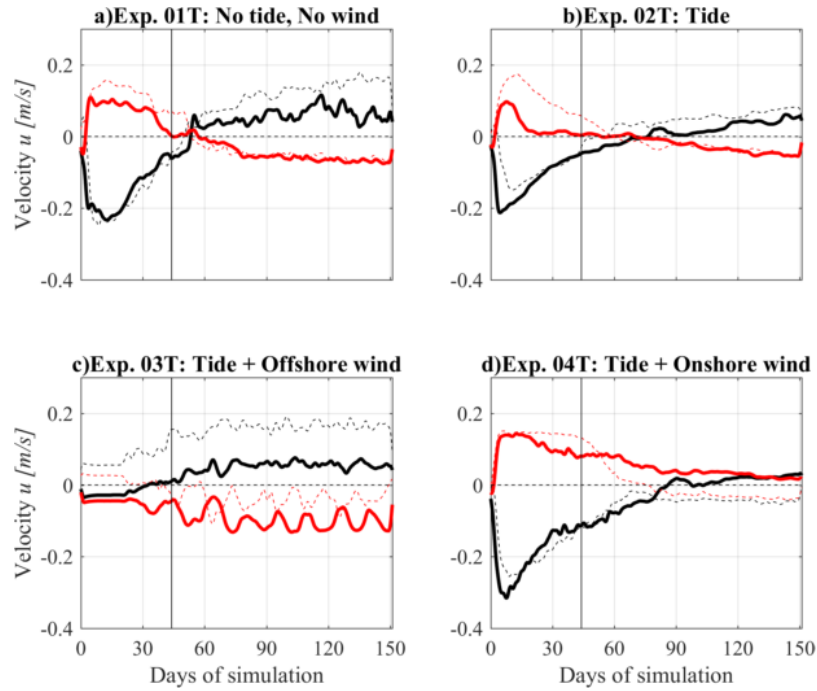
545

546

547

548

549



550

551

552 Figure 6. Same as Figure 3 but for experiments with two inlets. Velocity is positive seaward.

553 Surface (black) and bottom (red) subtidal along-estuary velocities centered at the

554

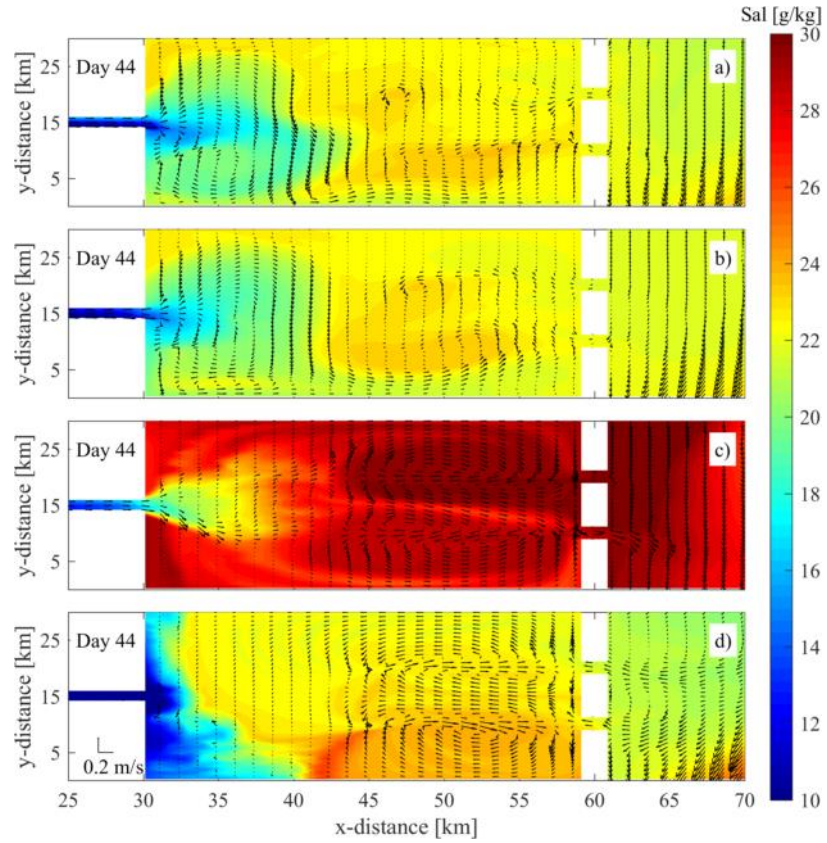
northern (solid lines) and the southern (dashed lines) inlets. The vertical solid line

555

denotes the time used for Figure 7.

556

557



558

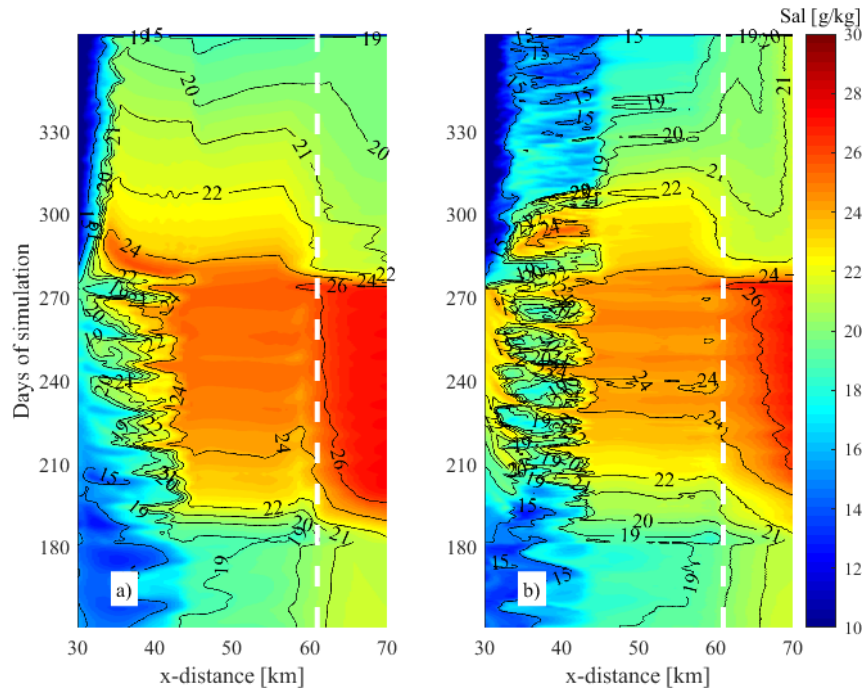
559 Figure 7. Experiments 1T to 4T. Surface fields of salinity (contour colors), and horizontal
560 velocity (arrows) averaged over one tidal cycle.

561

562

563

564



565

566

567 Figure 8. Hovmöller diagrams of along-estuary surface salinity for experiment 5 with the tide
568 and a non-stationary wind for a) northern inlet, and b) southern inlet. The time starts
569 from day 150 because before that time the longitudinal salinity was the same as the
570 experiment only with tides.

571

572

573

574

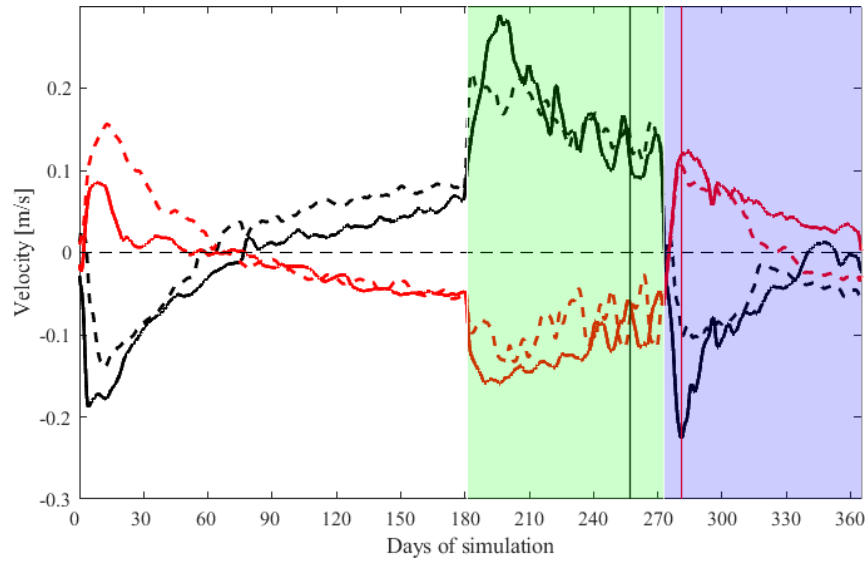
575

576

577

578

579



580

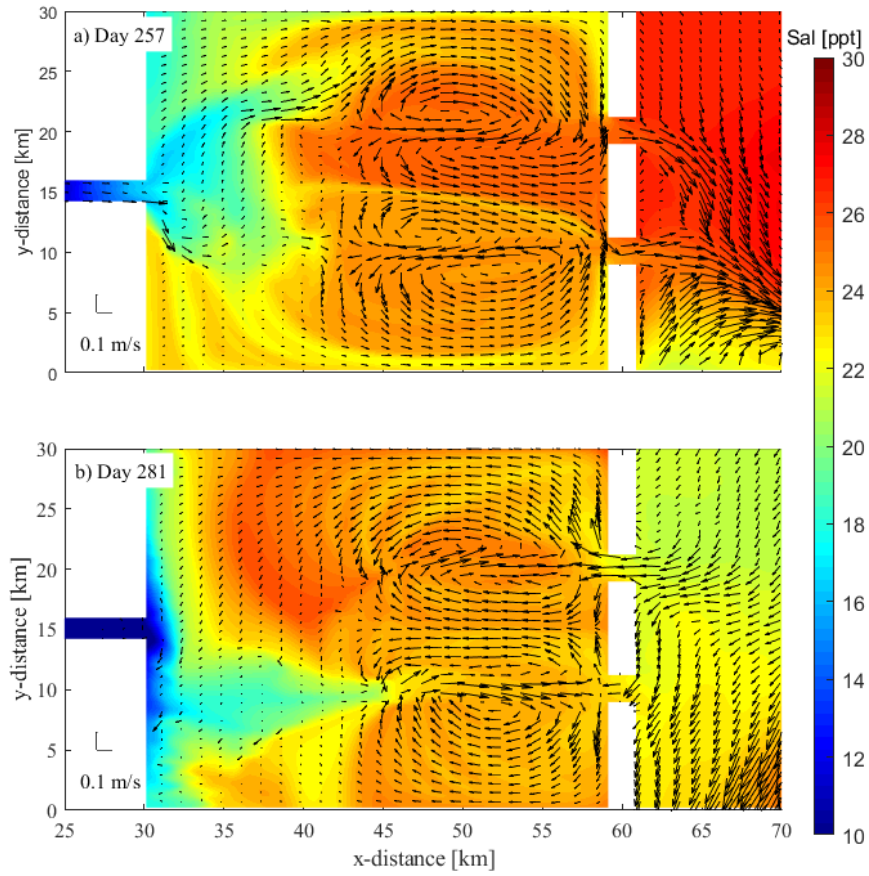
581

582 Figure 9. Experiment 5, with tide and a non-stationary wind. Surface (black) and bottom (red)
 583 subtidal along-estuary velocities centered at the northern (solid line) and southern
 584 (dashed line) inlet during the experiments with a non-stationary coastal current. The
 585 green rectangle denotes the period when the buoyant coastal current was turned off
 586 and an offshore wind was prescribed. The blue rectangle covers the period when the
 587 buoyant current was turned on and the wind direction reversed to onshore. The
 588 vertical black and red lines indicate, respectively, simulation day 257 and 281, whose
 589 salinity and velocity maps are shown in Figure 10.

590

591

592

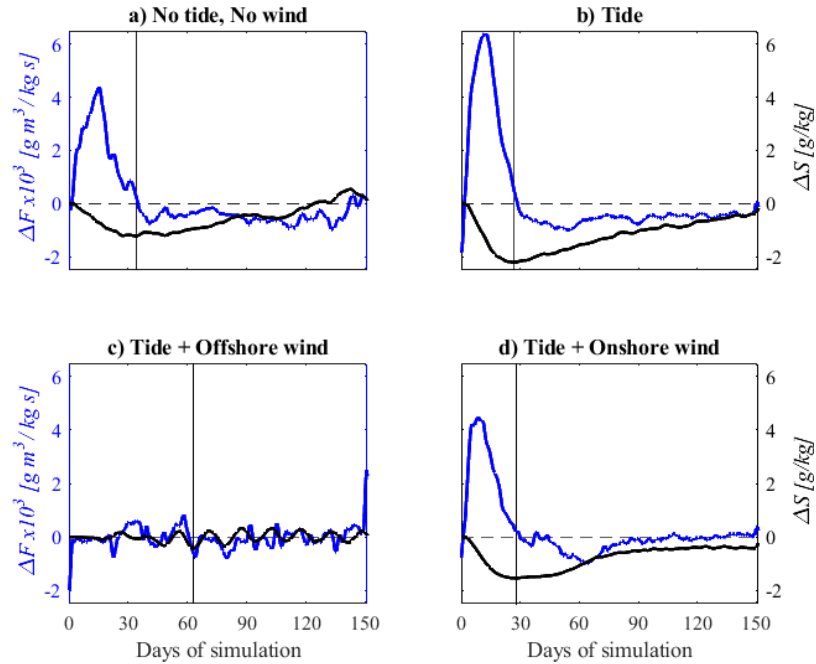


593

594

595 Figure 10. Experiment 5. Surface fields of salinity (contour colors), and horizontal velocity
596 (arrows) averaged over one tidal cycle when the buoyant current was turned off and
597 with offshore wind (a) and when it was turned on and the wind reversed to onshore
598 (b). See Figure 9.

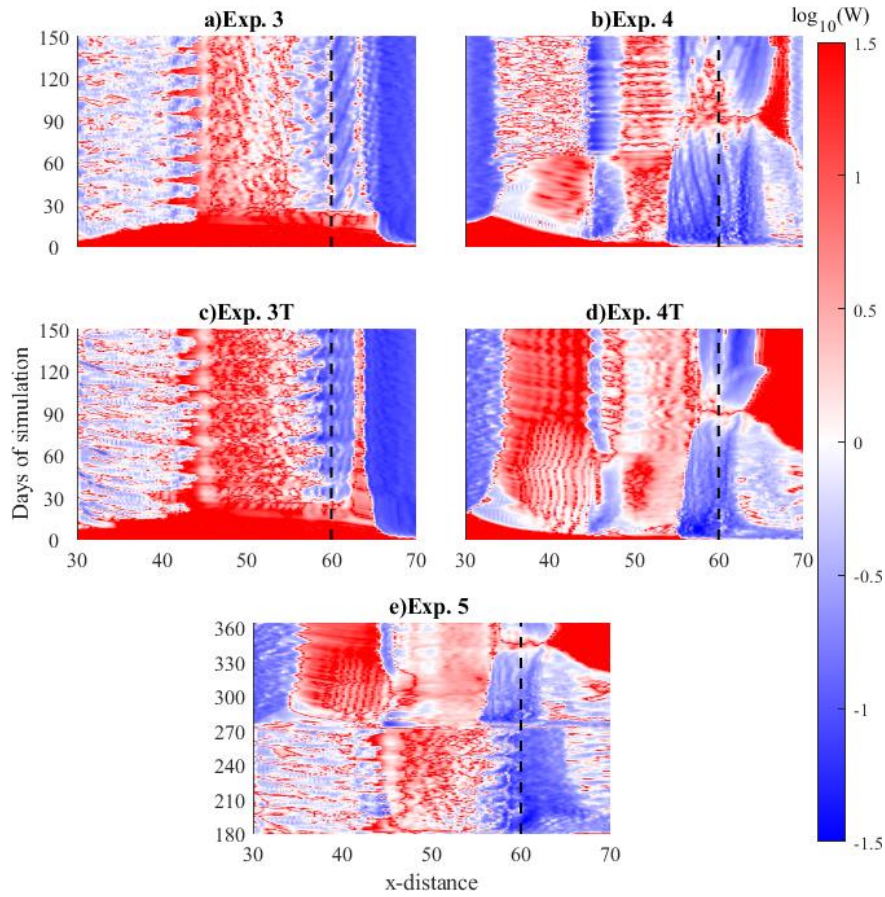
599



600
601
602
603
604
605
606
607

608
609
610

Figure 11. Salt flux difference between cases with two inlets and one inlet (ΔF [$\times 10^3 g m^3 / kg s$], blue line) and ΔS ($[g/kg]$, black line) for experiments with (a) no tide no wind, (b) with tide, (c) tide and offshore wind, and (d) tide and onshore wind. The vertical black line denotes the time with the minimum ΔS , which coincides with the time when salt fluxes were similar for cases with one and two inlets (i.e., when $\Delta F \sim 0$).



611
612

613 Figure 12. Hovmöller diagrams of the logarithm (\log_{10}) of Wedderburn number (W) calculated
 614 for experiments with cross-shore wind forcing, centered along the thalweg from the
 615 bay head ($x = 30$ km) to the inlet ($x = 60$ km, vertical black dashed line). The
 616 northern inlet was used for cases with two inlets (Experiments 3T, 4T, and 7, c, d, and
 617 e respectively). Blue color denotes $\log_{10}(W) < 0$ consequently dominance of the
 618 density gradients and red color denotes $\log_{10}(W) > 0$ which indicates that wind
 619 stresses govern over the density gradients.